How to cite: *Angew. Chem. Int. Ed.* **2024**, e202317058
doi.org/10.1002/anie.202317058

Alloy Electrocatalysts

Transpassive Metal Dissolution vs. Oxygen Evolution Reaction: Implication for Alloy Stability and Electrocatalysis

*Annica Wetzel, Daniel Morell, Marcus von der Au, Gunther Wittstock, Ozlem Ozcan, and Julia Witt**

Abstract: Multi-principal element alloys (MPEAs) are gaining interest in corrosion and electrocatalysis research due to their electrochemical stability across a broad pH range and the design flexibility they offer. Using the equimolar CrCoNi alloy, we observe significant metal dissolution in a corrosive electrolyte (0.1 M NaCl, pH 2) concurrently with the oxygen evolution reaction (OER) in the transpassive region, despite the absence of hysteresis in polarization curves or other obvious corrosion indicators. We present a characterization scheme to delineate the contribution of OER and alloy dissolution, using scanning electrochemical microscopy (SECM) for OER-onset detection, and quantitative chemical analysis with inductively coupled-mass spectrometry (ICP-MS) and ultraviolet visible light (UV/Vis) spectrometry to elucidate metal dissolution processes. In situ electrochemical atomic force microscopy (EC-AFM) revealed that the transpassive metal dissolution on CrCoNi is dominated by intergranular corrosion. These results have significant implications for the stability of MPEAs in corrosion systems, emphasizing the necessity of analytically determining metal ions released from MPEA electrodes into the electrolyte when evaluating Faradaic efficiencies of OER catalysts. The release of transition metal ions not only reduces the Faradaic efficiency of electrolyzers but may also cause poisoning and degradation of membranes in electrochemical reactors.

[*] A. Wetzel, D. Morell, Dr. M. von der Au, Dr.-Ing. O. Ozcan, Dr. J. Witt
Bundesanstalt für Materialforschung und Prüfung (BAM) Institution
Unter den Eichen 87
12205 Berlin (Germany)
E-mail: julia.witt@bam.de

A. Wetzel, Prof. Dr. G. Wittstock
Institute of Chemistry
Carl v. Ossietzky Universität Oldenburg
Ammerländer Heerstrasse 114–118
26129 Oldenburg (Germany)

Introduction

Multi-principal element alloys (MPEAs) are currently in the spotlight as emerging structural materials[1] and electrocatalysts, particularly as electrodes for the oxygen evolution reaction (OER) in electrolyzers.[2] Their attractiveness results, among other factors, from their mechanical robustness and resistance to corrosion at high anodic potentials.[1a,3] More recent research into their electrocatalytic properties promises potential for OER applications which bestows an even higher significance on MPEA materials as they are generally composed of earth-abundant non-noble transition metals.[4]

These advantageous properties are rooted in the transpassive electrochemical behavior of MPEAs. The transpassive behavior of metals is generally more complex than their electrochemical properties in the active and passive states. This complexity arises because various mechanisms can contribute to Faradaic currents in the transpassive state, specifically, metal dissolution and OER.[5] Under the effect of the high electric field in the passive film, ions (metal cations, O^{2-}, other anions) can participate in charge transfer reactions. The resulting conductivity of the passive layer may be influenced by defects of different kinds in the passive film. Furthermore, the breakdown of the passive film can occur through various mechanisms. The competition between consumption and reformation of the passive film may cause a steady state. Additionally, OER goes along with local changes in pH and in ionic composition of the solution near the electrode that feeds back on passive film formation and breakdown. A fundamental difficulty in analyzing these scenarios is the lack of operando techniques that allow the establishment of structure–reactivity relationships under the specific reaction conditions. The challenge becomes even greater because many of the above-mentioned processes do not occur uniformly over the metal surface but are associated with defects on different size regimes, such as dislocations, grain boundaries, inclusions, and corrosion pits.

The concomitant occurrence of the OER and metal dissolution during high anodic polarization in the transpassive potential region is a known phenomenon. It not only limits the stability of structural elements made from MPEAs[6] but also poses a challenge in identifying active and stable electrocatalysts.[5b,7] While both processes contribute to the experimentally observed current density, a vast majority of studies have focused either on the OER activity or the stability of the electrocatalyst towards corrosion.[2b,c,4,8]

Recent research suggests an inevitable link between the OER and material dissolution.[5a] A thorough understanding of the transpassive behavior of metallic surfaces and metal nanoparticle-based electrocatalysts is of crucial importance to evaluate the performance of materials and to achieve a mechanistical understanding of degradation processes defining their stability.

Typical corrosion studies involve analyzing polarization curves (I vs. E at low scan rates, v), employing electrochemical impedance spectroscopy (EIS) complemented by ex situ analyses of the metallic surface in the pre- and post-corroded states. However, there is only a very limited number of methods available for real-time analysis of corrosion, especially at localized corrosion sites. In polarization experiments in aqueous environments, high anodic potentials can lead to current densities, often attributed not only to passivity breakdown but also to the OER.[5a,9] Atomic spectroelectrochemistry has emerged as a suitable approach to investigate selective metal dissolution during corrosion.[10] This approach can utilize flow-type scanning droplet (or capillary) cell microscopies,[11] coupled with inductively coupled plasma (ICP) atomic emission spectrometry (ICP-AES),[12] and/or ICP mass spectrometry (ICP-MS).[13] Cherevko and Mayrhofer et al.[5a] demonstrated, by means of scanning flow cell ICP-MS, that even noble metal catalysts (e.g., Au or Pt) exhibit seemingly good OER activities at low overpotentials but dissolve considerably during polarization. Ott et al.[13c] have applied microcapillary plasma mass spectrometry to investigate the passive state of the Al-Cr-Fe γ-phase and reported a preferential over-stoichiometric dissolution of Al and Fe cations and an enrichment of Cr in the passive film in a sulfuric acid electrolyte. The transpassive dissolution of pure Cr was investigated in 0.1 M NaCl using atomic spectroelectrochemistry by Birbillis and co-workers.[14] Their real-time dissolution analysis showed the oxidative dissolution of the Cr_2O_3 passive film directly to Cr(VI) in the transpassive potential region.

While online atomic spectroelectrochemistry provides instant monitoring of metal dissolution during corrosion, the simultaneous detection and quantification of other stoichiometrically relevant electron transfer processes, such as the H_2 evolution reaction (HER) or OER have remained elusive. Ogle and co-workers[15] quantified H_2 evolution during Mg corrosion using online time-resolved volumetry and online atomic spectroelectrochemistry. Using online atomic spectroelectrochemistry, Wen et al.[16] demonstrated more recently an accurate ascription of anodic current contribution of OER at a carbon-supported Ru-based catalyst and distinguished it from other contributions arising from side reactions (such as catalyst dissolution or support degradation).

Scanning probe techniques such as electrochemical atomic force microscopy (EC-AFM) and scanning electrochemical microscopy (SECM) serve as valuable tools for the analysis of local corrosion phenomena. EC-AFM has been applied in various contexts ranging from monitoring surface roughening, imaging local pit initiation to detecting electrocatalytically active sites on electrocatalysts for the OER or the oxygen reduction reaction (ORR).[17] Even though EC-AFM captures in situ topographical changes, it lacks the capability to detect specific compositional information and is mostly insensitive to electron transfer reactions. SECM in the sample-generation/tip-collection (SG/TC) mode can be operated in a chemically selective way by setting the probe potential to oxidize or reduce a compound that is generated at reactive sites on the sample, such as grain boundaries or active local corrosion sites.[18] For instance, Souto et al.[19] employed SECM in the SG/TC mode to monitor the emergence of Fe(II) and O_2 at anodic sites from corroding coated carbon steel by means of horizontal line scans. Here, we employ tip-substrate voltammetry (TSV) in the SG/TC mode (TSV-SECM), in which the microelectrode (ME) of the SECM is used to detect products of the sample electrode, while conducting a voltammetric scan at the sample.[18c,20] Similar to our approach, Matysik et al.[21] demonstrated the advantage of using hydrodynamic TSV-SECM to detect the evolution of reactive oxygen species (e.g., $OH^{\bullet}$, H_2O_2 or O_2^-) on Pt and boron-doped diamond macroelectrodes. The combination of EC-AFM and SECM has been employed to obtain simultaneously local topographical and electrochemical information.[22]

Using equimolar CrCoNi as a model MPEA, we present a comprehensive methodology to identify the onset of the OER and to distinguish it from metal dissolution. The aim is to gain a deeper understanding on the contributions to the transpassive current density arising from corrosive and electrocatalytic reactions. The studies are conducted in an acidic Cl^--containing electrolyte. Results of other electrolytes are briefly covered at the end of the manuscript. Our approach combines TSV-SECM, elemental analysis, and EC-AFM. CrCoNi is resistant to general and pitting corrosion.[23] However, our recent investigations revealed that the alloy is susceptible to intergranular corrosion at high anodic potentials in the transpassive region.[24] Further analysis showed minimal metal dissolution due to transpassive dissolution, suggesting a contribution of the OER to the observed anodic current density.

Results and Discussion

We apply TSV-SECM (Figure 1A) to record a polarization curve of the CrCoNi sample and simultaneously monitor the evolution of O_2 from the sample by its detection at the ME. The ME is positioned 5 μm above the CrCoNi sample and polarized at $E_T = -0.65$ V for amperometric detection of O_2 (Figure 1A, top). All electrode potentials in this paper are reported against Ag/AgCl/3 M NaCl. For other experimental details, please refer to the Experimental Procedure section in the Supporting Information (SI-1, Figure S1–S3). The chemical composition of CrCNi is listed in Table S1. The cyclic voltammetry (CV) is recorded at the alloy sample at low scan rates to ensure steady-state conditions. In the field of corrosion, this experiment at the sample is commonly known as cyclic potentiodynamic polarization (CPP) and is plotted in a semilogarithmic form (Figure 1B, bottom). To highlight the correlation to the ME currents,

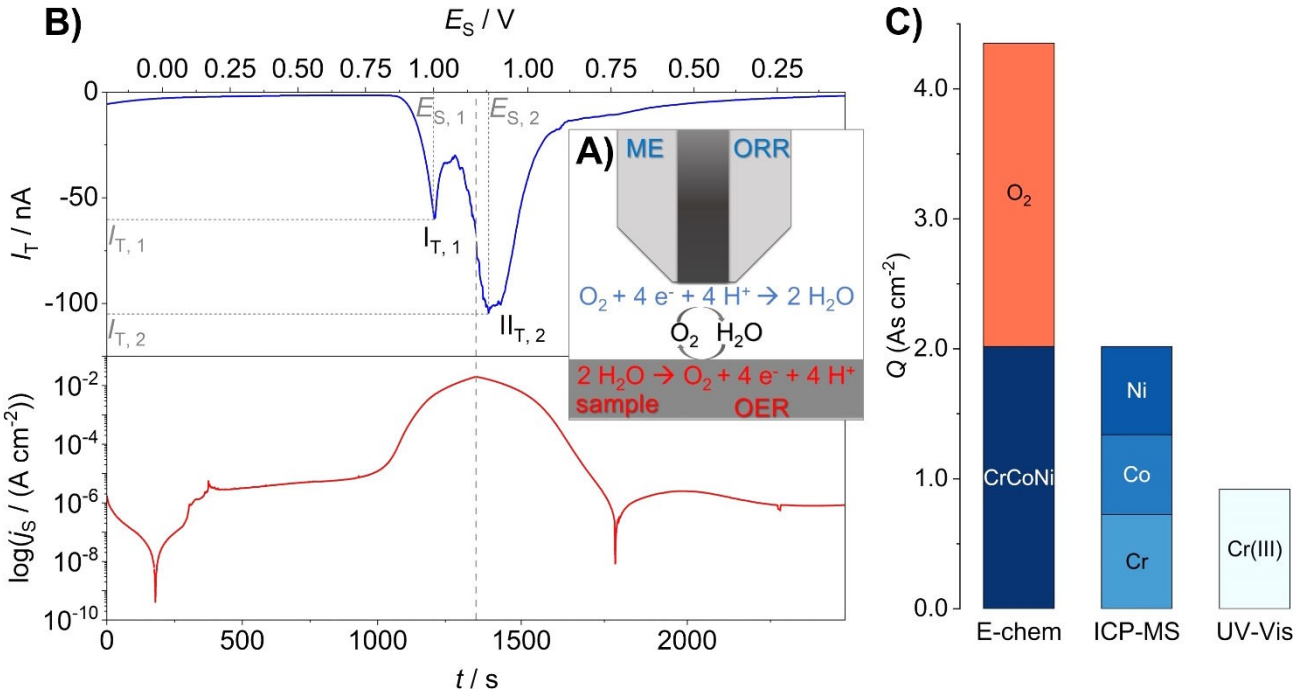

Figure 1. (A) Schematic of the ME and CrCoNi sample configuration for TSV; (B) TSV scan recorded at the CrCoNi substrate (bottom) at 1 mV s^{-1} and the simultaneously measured current at the ME (top) at −0.65 V vs. Ag/AgCl/3 M NaCl for the reduction of oxygen evolved at the CrCoNi sample in 0.1 M NaCl pH 2; (C) charges normalized to geometric electrode area as retrieved from the electrochemical, ICP-MS and UV/Vis measurements.

the voltammetric signals are plotted vs. time in Figure 1A, with the potentials of the CV scan at the sample indicated at the top of the plot.

Two distinctive peaks ($I_{T,1}$ and $II_{T,2}$) are observed in the ME response at the sample potentials of $E_{S,1} = 1.00$ V and $E_{S,2} = 1.15$ V (corresponding to 1206 s and 1410 s in Figure 1B (bottom), respectively). For comparison, the respective pure metals have also been investigated by TSV-SECM and ICP-MS quantification (SI-2.1 to SI-2.3, Figures S4–S6, Tables S2 and S3). The results showed that pure Cr exhibited a behavior similar to CrCoNi (Figure S4), with the two current peaks at the ME shifted by 0.15 V to higher potentials for pure Cr. This observation raises the possibility that Cr ions dissolved from the MPEA may also be reduced at the ME, in addition to the reduction of O_2 generated at the sample.

To address this possibility, a related MPEA, CrFeMnCoNi, was studied by TSV-SECM (Figure S7). This alloy shows metal dissolution at high anodic potentials as confirmed by ICP-MS quantification (Table S4). However, no ME response could be observed, indicating that no Cr is detected at the chosen ME potential (Figure S7). Based on these control experiments, it can be excluded that the reduction reactions of Cr(III), Ni(II) and Co(II) to the respective metals significantly contribute to the measured ME current. Additional CPP measurements conducted on FeCrNi in a 0.1 M NaCl electrolyte solution showed that the electrochemical behavior of FeCrNi MPEA is comparable to that of CrCoNi (SI-2.5, Figure S8). This result suggests that the superior OER activity and reduced metal dissolution observed in CrCoNi, compared to the pure metal, cannot be solely attributed to the presence of CoNi.

The presence of the first reduction peak $I_{T,1}$ in the TSV ME response, observed for both CrCoNi ($E_{S,1} = 1.00$ V) and Cr ($E_{S,1} = 1.15$ V), is an intriguing observation with excellent reproducibility. At the tip-to-substrate distance of $d = 5$ µm in TSV-SECM, a local thin-layer cell is formed, in which the diffusion of species into and away from the cell is hindered. While bubble formation in the thin-layer cell could potentially affect the ME response and local current density distribution, no bubble formation was visually observed. Furthermore, bubbles would cause an immediate drop of the ME current, which was not observed in our experiments. Thus, any influence of bubble formation or detachment on the mass transport of dissolved species in the thin-layer cell can be ruled out. The increasing anodic polarization of the substrate in the forward scan is expected to yield a single peak at the ME, with maximum current density at or shortly after the apex potential of the TSV scan at the sample. This is attributed to the finite transition time of O_2 from the sample to the ME, a factor deemed negligible against the time scale of the potential scan at the sample with $v = 1$ mV s^{-1}.[25]

During the backward scan of the TSV-SECM, the CrCoNi MPEA surface effectively repassivates to a current density of ~0.8 µA cm^{-2}, which is significantly lower than the primary passivation current density of ~4.0 µA cm^{-2} (Figure 1B). In this context, it should be noted that the UV/Vis spectroscopic analysis (Figure 1C) revealed that all chromium species present after the TSV scans were in the Cr(III)

state. This suggests the possibility that transpassively produced Cr(VI) may have been reduced upon the TSV reversal. Examining the anodic Tafel slopes in Figure S9 of 42 mV dec^{-1} and 55 mv dec^{-1} for Cr and CrCoNi, respectively, and comparing them to results obtained for noble metal catalysts,[5a] implies a potential prediction for the transformation of oxides from the oxide layer to oxygen for the OER [Equation (S1)] in concomitance with metal dissolution. Higher slopes (approx. > 120 mV dec^{-1}) may indicate preferential oxidation of adsorbed water [Equation (S2)].[5a,26] In contrast to the MPEA, Cr(VI) is still present after the TSV of pure Cr (Table S5), indicating a difference in the mechanism by which the oxide layer participates in the OER (as further discussed in SI-2.6).

The analysis of the metal ion concentration in the electrolytes after electrochemical measurements was performed by means of ICP-MS (details in SI-1.7). To ensure accurate conversions of the determined metal concentration into charge, the number of exchanged electrons, n_{Me} (Me = Co, Ni, Cr) must be considered. While the dissolution reactions of Co and Ni proceed with $n_{Co} = n_{Ni} = 2$,[27] the dissolution of Cr could occur with $n_{Cr} = 3$ or $n_{Cr} = 6$.[28] During the electrochemical measurements on pure Cr substrates, the electrolyte turned bright yellow, and the electrolytes of the CrCoNi sample also showed a faint yellow hue after constant polarization at $E_{S,2}$ (1.15 V). At this potential, the second ORR peak ($II_{T,2}$) is recorded at the ME, suggesting the presence of Cr(VI) species. UV/Vis analyses of Cr(VI) species in the electrolytes after TSV-SECM were performed according to SI-1.8 and are summarized in Table S5. The average number of exchanged electrons n_{Cr} was calculated according to Equation (S4) and then employed to calculate the converted charge [Equation (1)] for metal dissolution using the metal concentrations $c_{Me,ICP}$ (Me = Co, Ni, Cr) as measured by ICP-MS (data in SI-2.8, Table S6).

$$Q_{Me} = \left(c_{Cr,ICP} n_{Cr} + c_{Co,ICP} n_{Co} + c_{Ni,ICP} n_{Ni}\right) FV \quad (1)$$

Here $V = 0.01$ L is the solution volume and $F = 96485$ As mol^{-1} is the Faraday constant. Subtraction of Q_{Me}, from the total charge Q_{echem} yields the charge Q_{O2} expended for the OER (Table 1).

Assuming that O_2 evolving from the alloy sample is detected by the ME at both peaks in the upper panel of Figure 1A, chronoamperometric measurements with subsequent ICP-MS and UV/Vis analysis were performed on the CrCoNi MPEA and pure Cr specimen at the respective peak potentials for a duration of 30 min to determine steady-state transpassive currents. During anodic polarization of CrCoNi, current densities of ~5 mA cm^{-2} at $E_{S,1} = 1.00$ V and ~20 mA cm^{-2} at $E_{S,2} = 1.15$ V were observed in Figures S10A and S10B. On the pure Cr specimen, the current density was ~6 mA cm^{-2} at $E_{S,1} = 1.15$ V and increased to ~15 mA cm^{-2} at $E_{S,2} = 1.30$ V (Figures S11A and S11B). Derived charges for the respective corrosive dissolution of metals and catalytic OER are summarized in Table 1. The highest Faradaic efficiency $\varepsilon(O_2) = 53\,\%$ is found for CrCoNi after TSV-SECM. Figure 1C presents the

Table 1: Total charges and charge contribution from metal dissolution in 0.1 M NaCl pH 2 and OER curing constant polarization experiments of CrCoNi for 30 min. The presented data are the average and standard deviations of 3 replicate experiments. The charges are normalized to the geometric electrode area. Faradaic efficiencies $\varepsilon(O_2)$ are given for the OER ($Q_{O2}/Q_{e\text{-}chem}$).

Sample	$Q_{e\text{-}chem}$	$Q_{Met(ICP)}$	Q_{O_2}	$\varepsilon(O_2) = Q_{O_2}/Q_{e\text{-}chem}$
	[As cm^{-2}]	[As cm^{-2}]	[As cm^{-2}]	[%]
CrCoNi $_{TSV}$	4.35 ± 0.35	2.02 ± 0.38	2.33 ± 0.38	53.46 ± 4.36
CrCoNi $I_{T,1}$	8.95 ± 1.54	5.71 ± 0.90	3.23 ± 0.65	36.01 ± 1.35
CrCoNi $II_{T,2}$	34.97 ± 0.85	25.35 ± 1.16	9.62 ± 1.77	27.46 ± 4.57
Cr $_{TSV}$	4.35 ± 0.20	2.65 ± 0.26	1.16 ± 0.06	30.62 ± 3.25
Cr $I_{T,1}$	10.75 ± 0.24	8.78 ± 0.43	1.97 ± 0.20	18.37 ± 2.23
Cr $II_{T,2}$	25.60 ± 1.24	20.44 ± 0.46	5.16 ± 0.78	20.11 ± 2.09

expended charges (normalized by the geometric sample area) for the metal dissolution and OER on CrCoNi after the entire TSV-SECM experiment. The $\varepsilon(O_2)$ value after chronoamperometry is slightly higher at the potential $E_{S,1}$ of the first ME peak ($I_{T,1}$) than at the potential $E_{S,2}$ of the second ME peak ($II_{T,2}$). The main difference between the chronoamperometric tests and TSV-SECM scans is likely due to the anodic passivation during the voltammetric scan. If the OER predominantly proceeds through oxidation of passive layer oxides, the formation of a thicker oxide layer on the CrCoNi surface during TSV-SECM experiments inhibits metal dissolution and thus boosts the OER activity.

Figure 2A and B summarize the results from the chronoamperometric measurements. The findings for CrCoNi reveal that, during the polarization at $E_{S,1} = 1.00$ V, a significantly higher concentration of Cr(III) is present compared to polarization at $E_{S,2} = 1.15$ V. In the case of the pure Cr specimen, only a minute amount of Cr(III) was detected, and the concentration ratio of Cr(III) to Cr(VI) showed no significant difference between the polarization at $E_{S,1} = 1.15$ V and $E_{S,2} = 1.30$ V. Considering the similar current density traces of the CrCoNi MPEA and pure Cr samples measured during the chronoamperometric scans (Figures S10 and S11), the fraction of charge transferred for Cr dissolution is threefold higher at the pure Cr specimen than on CrCoNi during polarization at the $E_{S,1}$ (Table S7).

The results of the chronoamperometric measurements at $E_{S,1}$ for 10 h on CrCoNi and Cr (Figure S12) indicate that Cr experiences sole dissolution and lacks long-term stability (Table S8). The Faradaic efficiency of CrCoNi for the OER exceeds $\varepsilon(O_2) = 20\,\%$ (Table S8). Considering that the MPEA surface was polarized for 10 h without prior anodizing treatment, there is potential for further enhancement in Faradaic efficiency.

To gain more insights into the local phenomena, in situ corrosion studies were conducted using EC-AFM (Figure 3A) to investigate the evolution of topography of the CrCoNi surface during CPP (Figure 3B) with intermittent image recording (I to IV) at the indicated potentials of

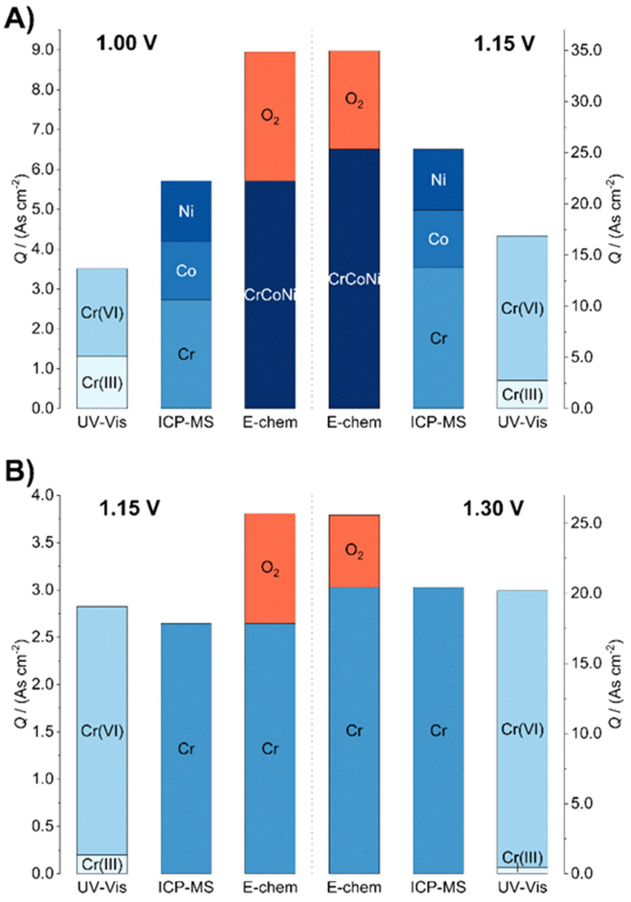

Figure 2. The geometric surface area-normalized charges determined via ICP-MS and UV/Vis spectrometry in comparison with the charge calculated for O_2 evolution from the chronoamperometric analysis in 0.1 M NaCl pH 2 at the indicated potentials on (A) CrCoNi MPEA and (B) pure Cr specimen.

0.00 V, 0.40 V, 0.85 V, and 1.15 V. The EC-AFM images in Figure 3C demonstrate that the morphology of the CrCoNi surface remained essentially unchanged and stable between 0.00 V and 0.85 V (Figure 3B, panels I to III). Notably, significant topographical changes were neither observed in the twin structures (Figure 3C, panel I, marker a), at grain boundaries (Figure 3C, panel I, marker b), nor near inclusions (Figure 3C, panel I, marker c). Morphology changes due to corrosion were only detected at high anodic potentials (1.15 V), predominantly manifested in intergranular corrosion (Figure 3C, panel IV, marker e) and minimal pitting (Figure 3C, panel IV, marker d). The surface roughness of the CrCoNi substrate increased after polarization at 1.15 V (Figure S13), indicating the formation of a transient transpassive film.

To further investigate the properties of the metal surface, EIS was measured, as described in SI-2.12. Two different electrical equivalent circuits (EECs) were used to model the behavior of the CrCoNi electrode (Figure S14). The obtained data are presented in Figures S15 to S20. Based on previous studies on stainless steels,[9a,29] the CrCoNi alloy seems to exhibit a high corrosion resistance without undergoing an apparent secondary passivation in the transpassive regime.[30] At polarizations below the transpassive region (−0.25 to 0.40 V), the EIS data in Figures S15, S16 and S17 indicate a perfectly passivated metal surface with a magnitude of the impedance $|Z| = 0.25\ M\Omega\,cm^2$ at 0.1 Hz. At transpassive polarizations (1.00 V and 1.15 V), Figures S18C and S19 C exhibit an inductive loop in the Nyquist plots, and the currents are mainly impeded by the solution resistance, suggesting increased ion conductivity of the oxide film.[29] Moreover, the low-frequency impedance at 0.01 Hz decreases significantly by four orders of magnitude compared to the polarization below 1.0 V, indicating a low charge transfer resistance at the CrCoNi electrode. Interpreted together with the EC-AFM results, the low charge transfer resistance and strong inductive response in the EIS data suggest a lack of a passive/transpassive oxide film or an oxide film that catalyzes the OER. Direct homogeneous dissolution on the grain surfaces cannot be excluded.

The maximum ME current of the first peak ($I_{T,1}$) coincides with the potential where a change of the slope of the sample current density trace is observed. Considering the EC-AFM studies, a plausible explanation could be the transition from the dynamic transpassive film growth and dissolution to intergranular corrosion where dissolved Cr-(VI) species in crevices at grain boundaries cannot diffuse to the solution as fast as the species originating from the flat surface. The transpassive film growing at potentials below 1.0 V appears to offer a limited barrier function to metal dissolution until intergranular corrosion becomes the dominant mode at potentials positive of 1.0 V.

The transpassive behavior of metals depends not only on the chemical composition of the metal but also on the corrosion medium. As an example, we also tested the behavior in artificial seawater and in a chloride-free sulfate electrolyte (see discussion in SI-2.12). The CrCoNi MPEA shows a stable behavior with high anodic currents in the transpassive potential range and good repassivation behavior in artificial seawater (Figure S21). In Cl^--free sulfate electrolyte at pH 2, the onset of OER is shifted to more positive potentials (Figure S22), while the Faradaic efficiency for OER is approximately $\varepsilon(O_2) = 40\,\%$ (Table S9). The significant change in the transpassive behavior may be attributed to the incorporation of sulfate into the passive film, altering both, the stability against metal dissolution and the electrocatalytic properties for OER.

In addition to evaluating the stability of MPEA in corrosive environment or assessing the activity of MPEA electrocatalysts, the dissolution of MPEA electrodes can have significant impact on electrolyzers. The conductivity of proton-exchange membranes (PEMs) in electrolyzers decreases significantly when dissolved Fe and Cr ions exceed threshold concentrations of 300 ppm and 200 ppm, respectively.[31] Moreover, the presence of various metal ions reduces the threshold values for each kind of ion, posing a potential challenge for non-noble multi-metal electrocatalysts.[2b,c, 31] Mo et al.[32] investigated the migration of transition metal cations into the membrane electrode assembly by using a model metal mesh of AISI 316 stainless

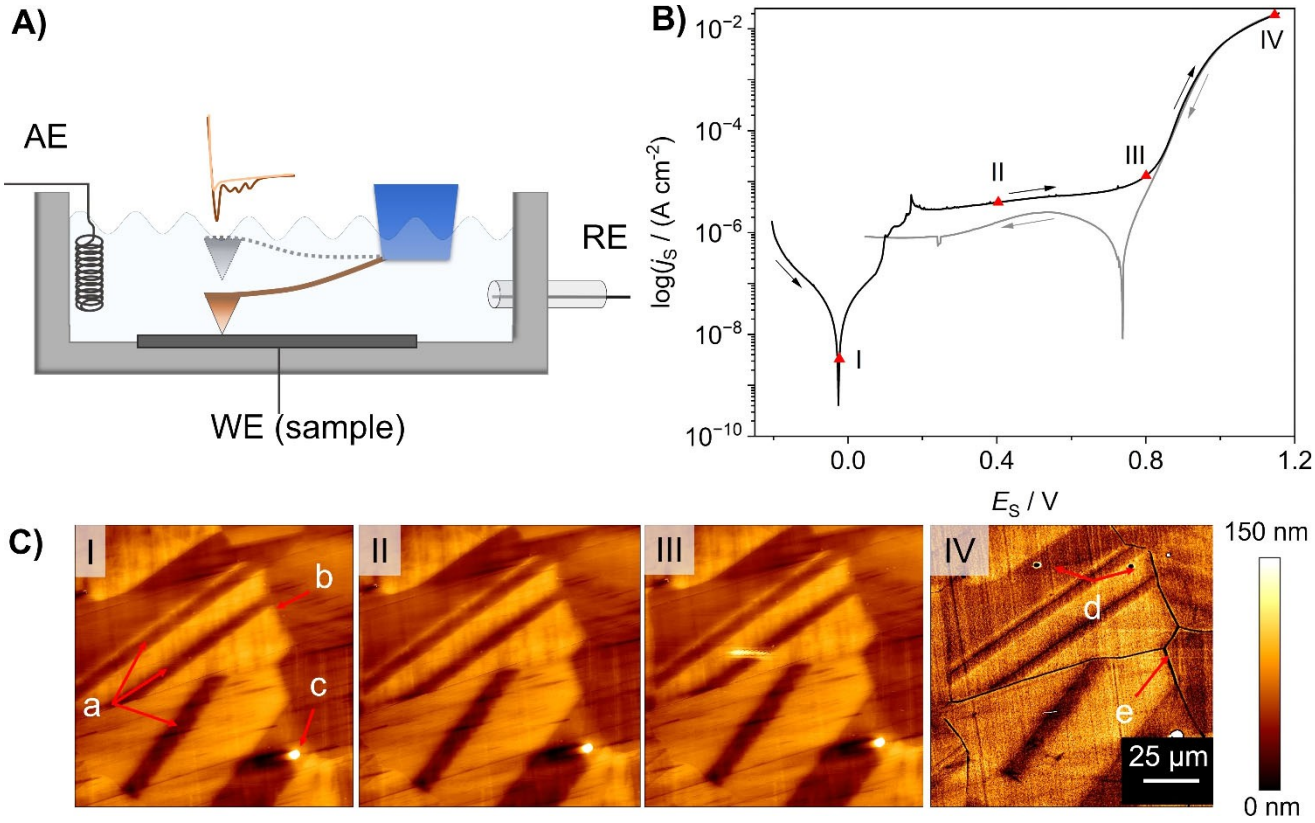

Figure 3. (A) Schematic setup of the EC-AFM experiment with the auxiliary electrode (AE), the reference electrode (RE) and the working electrode (WE); (B) Cyclic voltammogram of the CrCoNi sample in 0.1 M NaCl pH 2 from the TSV experiment (as shown in Figure 1) with indication of potentials for EC-AFM imaging (I, II, III and IV); (C) EC-AFM topography images collected at I) 0 V, II) 0.4 V, III) 0.85 V, and IV) 1.15 V vs. Ag/AgCl/3 M NaCl.

steel as the liquid/gas diffusion layer of a PEM electrolyzer cell and determined that the cation uptake proceeded in the order of Fe ≫ Ni ≫ Cr.[32b] For the CrCoNi alloy, the average total dissolved cation concentrations in Figure 1B are 31.42 ppm and 131.47 ppm after polarization at $E_{S,1}$ and $E_{S,2}$, respectively. The corresponding Cr concentrations were 8.5 ppm and 38 ppm and thus below the stated threshold values.

Given the growing interest in MPEAs for OER electrocatalysis, numerous catalyst chemistries have emerged.[33] To provide a comprehensive assessment of their potential, reporting on overpotentials and electrocatalytic activities should be complemented with data on the metal dissolution at the anode surface, a competing process to the OER that has been scarcely addressed thus far.[33c,34]

Conclusions

In conclusion, we have shown that significant OER takes places parallel to metal dissolution on the CrCoNi MPEA surface during anodic polarization in an acidic NaCl electrolyte at potentials relevant to water electrolysis. The alloy was chosen for this study due to its excellent corrosion and pitting resistance, along with low OER overpotential. To the best of our knowledge, this study is the first to distinguish between Cr(III) and Cr(VI) in the corrosion context, allowing the determination of metal dissolution and OER in the transpassive region.

By combining chemical analysis of the bulk electrolyte with the information obtained by means of TSV-SECM, we have illustrated the high corrosion resistance of CrCoNi without undergoing a secondary passivation. The growth and dissolution of the transpassive film can provide limited resistance to metal dissolution until grain boundary dissolution becomes the dominant corrosion mode. Ongoing studies by means of near ambient pressure X-ray photoelectron spectroscopy (NAP-XPS) shall clarify the formation and dissolution mechanisms of the transpassive film and provide information on its evolution at potentials relevant to water splitting. The absence of Cr(VI) after the TSV-SECM suggests the reduction of transpassively formed Cr(VI) to Cr(III), which requires further in-depth exploration. Most importantly, this study demonstrates that Faradaic efficiencies of non-noble metal OER electrocatalysts cannot be evaluated without the analysis of metal ions dissolved into the electrolyte.

Supporting Information

The authors have cited additional references within the Supporting Information (Ref. [35–56]).

Acknowledgements

The authors want to thank Prof. Guillaume Laplanche and co-workers from Ruhr-University, Bochum, Germany for providing the alloy materials. The authors greatly acknowledge funding from the Bundesanstalt für Materialforschung und -prüfung (BAM), Berlin, Germany through the PhD and PostDoc Program. Open access fees for this work were provided by BAM within the DEAL consortium. Open Access funding enabled and organized by Projekt DEAL.

Conflict of Interest

The authors declare no conflict of interest.

Data Availability Statement

The datasets used and/or analysed during the current study are available from the corresponding author on reasonable request.

Keywords: Multi-principal element alloys · Metal dissolution · Oxygen evolution reaction · Cyclic potentiodynamic polarization · Scanning electrochemical microscopy (SECM)

[1] a) E. P. George, D. Raabe, R. O. Ritchie, *Nat. Rev. Mater.* **2019**, *4*, 515–534; b) W. Chen, A. Hilhorst, G. Bokas, S. Gorsse, P. J. Jacques, G. Hautier, *Nat. Commun.* **2023**, *14*, 2856.

[2] a) T. Loffler, A. Ludwig, J. Rossmeisl, W. Schuhmann, *Angew. Chem. Int. Ed.* **2021**, *60*, 26894–26903; b) J. Zhang, T. Quast, W. H. He, S. Dieckhofer, J. R. C. Junqueira, D. Ohl, P. Wilde, D. Jambrec, Y. T. Chen, W. Schuhmann, *Adv. Mater.* **2022**, *34*, 2109108; c) I. A. Cechanaviciute, R. P. Antony, O. A. Krysiak, T. Quast, S. Dieckhofer, S. Saddeler, P. Telaar, Y. T. Chen, M. Muhler, W. Schuhmann, *Angew. Chem. Int. Ed.* **2023**, *62*, e2022184; d) H. J. Qiu, G. Fang, J. J. Gao, Y. R. Wen, J. Lv, H. L. Li, G. Q. Xie, X. J. Liu, S. H. Sun, *ACS Materials Lett.* **2019**, *1*, 526–533.

[3] L. Z. Medina, L. Molmen, E. M. Paschalidou, O. Donzel-Gargand, P. Leisner, U. Jansson, L. Nyholm, *Adv. Funct. Mater.* **2023**, 2307897.

[4] F. D. Speck, A. Zagalskaya, V. Alexandrov, S. Cherevko, *Angew. Chem. Int. Ed.* **2021**, *60*, 13343–13349.

[5] a) S. Cherevko, A. R. Zeradjanin, A. A. Topalov, N. Kulyk, I. Katsounaros, K. J. J. Mayrhofer, *ChemCatChem* **2014**, *6*, 2219–2223; b) A. Larsson, A. Grespi, G. Abbondanza, J. Eidhagen, D. Gajdek, K. Simonov, X. Q. Yue, U. Lienert, Z. Hegedus, A. Jeromin, T. F. Keller, M. Scardamaglia, A. Shavorskiy, L. R. Merte, J. S. Pan, E. Lundgren, *Adv. Mater.* **2023**, 2304621.

[6] S. Choudhary, S. Thomas, D. D. Macdonald, N. Birbilis, *J. Electrochem. Soc.* **2021**, *168*, 051506.

[7] a) T. Binninger, R. Mohamed, K. Waltar, E. Fabbri, P. Levecque, R. Kotz, T. J. Schmidt, *Sci. Rep.* **2015**, *5*, 12167; b) F. M. Li, L. Huang, S. Zaman, W. Guo, H. F. Liu, X. P. Guo, B. Y. Xia, *Adv. Mater.* **2022**, *34*, 2200840.

[8] a) G. L. Song, *Corros. Sci.* **2005**, *47*, 1953–1987; b) A. Fattah-Alhosseini, A. Saatchi, M. A. Golozar, K. Raeissi, *Electrochim. Acta* **2009**, *54*, 3645–3650.

[9] a) M. Bojinov, G. Fabricius, P. Kinnunen, T. Laitinen, K. Makela, T. Saario, G. Sundholm, K. Yliniemi, *Electrochim. Acta* **2002**, *47*, 1697–1712; b) E. Bettini, C. Leygraf, J. S. Pan, *Int. J. Electrochem. Sci.* **2013**, *8*, 11791–11804.

[10] a) S. Choudhary, K. Ogle, O. Gharbi, S. Thomas, N. Birbilis, *Electrochem. Sci. Adv.* **2022**, *2*, e2100196; b) X. J. Li, P. Zhou, H. Feng, Z. H. Jiang, H. B. Li, K. Ogle, *Corros. Sci.* **2022**, *196*.

[11] a) J. P. Kollender, M. Voith, S. Schneiderbauer, A. I. Mardare, A. W. Hassel, *J. Electroanal. Chem.* **2015**, *740*, 53–60; b) A. I. Mardare, J. P. Kollender, M. Hafner, A. W. Hassel, *Electrochem. Commun.* **2015**, *59*, 5–8.

[12] K. Ogle, S. Weber, *J. Electrochem. Soc.* **2000**, *147*, 1770–1780.

[13] a) M. M. Lohrengel, C. Rosenkranz, I. Kluppel, A. Moehring, H. Bettermann, B. Van den Bossche, J. Deconinck, *Electrochim. Acta* **2004**, *49*, 2863–2870; b) N. Ott, P. Schmutz, C. Ludwig, A. Ulrich, *Corros. Sci.* **2013**, *75*, 201–211; c) N. Ott, A. Beni, A. Ulrich, C. Ludwig, P. Schmutz, *Talanta* **2014**, *120*, 230–238.

[14] S. Choudhary, S. Zhang, S. Thomas, N. Birbilis, *ECS Adv.* **2022**, *1*, 011501.

[15] S. Lebouil, A. Duboin, F. Monti, P. Tabeling, P. Volovitch, K. Ogle, *Electrochim. Acta* **2014**, *124*, 176–182.

[16] J. H. Huang, S. B. Scott, I. Chorkendorff, Z. H. Wen, *ACS Catal.* **2021**, *11*, 12745–12753.

[17] a) J. Deng, M. R. Nellist, M. B. Stevens, C. Dette, Y. Wang, S. W. Boettcher, *Nano Lett.* **2017**, *17*, 6922–6926; b) J. T. Mefford, A. R. Akbashev, M. K. Kang, C. L. Bentley, W. E. Gent, H. T. D. Deng, D. H. Alsem, Y. S. Yu, N. J. Salmon, D. A. Shapiro, P. R. Unwin, W. C. Chueh, *Nature* **2021**, *593*, 67–73; c) S. H. Wang, Q. Jiang, S. H. Ju, C. S. Hsu, H. M. Chen, D. Zhang, F. Song, *Nat. Commun.* **2022**, *13*, 6650; d) T. K. Liu, C. H. Li, M. Olszta, J. H. Tao, A. Devaraj, *npj Mater. Degrad.* **2023**, *7*, 42.

[18] a) K. A. Lill, K. Fushimi, M. Seo, A. W. Hassel, *J. Appl. Electrochem.* **2008**, *38*, 1339–1345; b) M. Hampel, M. Schenderlein, C. Schary, M. Dimper, O. Ozcan, *Electrochem. Commun.* **2019**, *101*, 52–55; c) H. Bülter, G. Denuault, S. Matefi-Tempfli, M. Matefi-Tempfli, C. Dosche, G. Wittstock, *Electrochim. Acta* **2016**, *222*, 1326–1334.

[19] R. M. Souto, Y. Gonzalez-Garcia, S. Gonzalez, *Corros. Sci.* **2005**, *47*, 3312–3323.

[20] X. X. Chen, A. J. R. Botz, J. Masa, W. Schuhmann, *J. Solid State Electrochem.* **2016**, *20*, 1019–1027.

[21] C. Iffelsberger, T. Raith, P. Vatsyayan, V. Vyskocil, F. M. Matysik, *Electrochim. Acta* **2018**, *281*, 494–501.

[22] C. Kranz, G. Friedbacher, B. Mizaikoff, *Anal. Chem.* **2001**, *73*, 2491–2500.

[23] F. G. Coury, G. Zepon, C. Bolfarini, *J. Mater. Res. Technol.* **2021**, *15*, 3461–3480.

[24] A. Wetzel, M. von der Au, P. M. Dietrich, J. Radnik, O. Ozcan, J. Witt, *Appl. Surf. Sci.* **2022**, *601*, 154171.

[25] Y. Shen, M. Träuble, G. Wittstock, *Anal. Chem.* **2008**, *80*, 750–759.

[26] T. Shinagawa, A. T. Garcia-Esparza, K. Takanabe, *Sci. Rep.* **2015**, *5*, 13801.

[27] a) B. Beverskog, I. Puigdomenech, *Corros. Sci.* **1997**, *39*, 969–980; b) E. M. Garcia, J. S. Santos, E. C. Pereira, M. B. J. G. Freitas, *J. Power Sources* **2008**, *185*, 549–553.

[28] B. Beverskog, I. Puigdomenech, *Corros. Sci.* **1997**, *39*, 43–57.

[29] I. Betova, M. Bojinov, T. Laitinen, K. Makela, P. Pohjanne, T. Saario, *Corros. Sci.* **2002**, *44*, 2675–2697.

[30] A. I. Karayan, E. Maya-Visuet, H. Castaneda, *J. Solid State Electrochem.* **2014**, *18*, 3191–3202.
[31] H. L. Wang, J. A. Turner, *J. Power Sources* **2008**, *183*, 576–580.
[32] a) J. K. Mo, S. M. Steen, F. Y. Zhang, T. J. Toops, M. P. Brady, J. B. Green, *Int. J. Hydrogen Energy* **2015**, *40*, 12506–12511; b) J. K. Mo, S. Steen, Z. Y. Kang, G. Q. Yang, D. A. Taylor, Y. F. Li, T. J. Toops, M. P. Brady, S. T. Retterer, D. A. Cullen, J. B. Green, F. Y. Zhang, *Int. J. Hydrogen Energy* **2017**, *42*, 27343–27349.
[33] a) B. N. Khiarak, M. Mojaddami, Z. Z. Faradonbeh, A. O. Zekiy, A. Simchi, *Energy Fuels* **2022**, *36*, 4502–4509; b) W. W. Cao, X. Y. Yang, W. J. Dai, B. Wu, Y. D. Zhang, C. J. Zhao, Y. W. Sui, S. F. Huang, *New J. Chem.* **2023**, *47*, 12670–12677; c) A. Kumar, M. Mucalo, L. Bolzoni, Y. M. Li, Y. D. Qu, F. Yang, *Int. J. Hydrogen Energy* **2023**, *48*, 25755–25769; d) M. Mucalo, L. Bolzoni, Y. Qu, A. Kumar, Y. Li, F. Yang, *Mater. Today Sustain.* **2023**, *22*, 100360.
[34] J. Kwon, S. Sun, S. Choi, K. Lee, S. Jo, K. Park, Y. K. Kim, H. B. Park, H. Y. Park, J. H. Jang, H. Han, U. Paik, T. S. Song, *Adv. Mater.* **2023**, *35*, 2300091.
[35] G. Laplanche, A. Kostka, C. Reinhart, J. Hunfeld, G. Eggeler, E. P. George, *Acta Mater.* **2017**, *128*, 292–303.
[36] I. B. Butler, M. A. A. Schoonen, D. T. Rickard, *Talanta* **1994**, *41*, 211–215.
[37] G. Laplanche, S. Berglund, C. Reinhart, A. Kostka, F. Fox, E. P. George, *Acta Mater.* **2018**, *161*, 338–351.
[38] A. Wetzel, M. von der Au, P. M. Dietrich, J. Radnik, O. Ozcan, J. Witt, *Appl. Surf. Sci.* **2022**, *601*, 154171.
[39] a) S. Cherevko, A. R. Zeradjanin, A. A. Topalov, N. Kulyk, I. Katsounaros, K. J. J. Mayrhofer, *ChemCatChem* **2014**, *6*, 2219–2223; b) T. Binninger, R. Mohamed, K. Waltar, E. Fabbri, P. Levecque, R. Kotz, T. J. Schmidt, *Sci. Rep.* **2015**, *5*, 12167.
[40] a) L. H. Zhang, Q. Fan, K. Li, S. Zhang, X. B. Ma, *Sustain. Energy Fuels* **2020**, *4*, 5417–5432; b) K. X. Zhang, R. Q. Zou, *Small* **2021**, *17*, 2100129.
[41] L. T. Wang, D. Mercier, S. Zanna, A. Seyeux, M. Laurent-Brocq, L. Perriere, I. Guillot, P. Marcus, *Corros. Sci.* **2020**, *167*, 108507.
[42] L. G. Li, P. T. Wang, Q. Shao, X. Q. Huang, *Adv. Mater.* **2021**, *33*, 2004243.
[43] F. M. Li, L. Huang, S. Zaman, W. Guo, H. F. Liu, X. P. Guo, B. Y. Xia, *Adv. Mater.* **2022**, *34*, 2200840.
[44] A. Larsson, A. Grespi, G. Abbondanza, J. Eidhagen, D. Gajdek, K. Simonov, X. Q. Yue, U. Lienert, Z. Hegedus, A. Jeromin, T. F. Keller, M. Scardamaglia, A. Shavorskiy, L. R. Merte, J. S. Pan, E. Lundgren, *Adv. Mater.* **2023**, *35*, 2304621.
[45] H. Peng, J. Guo, G. Li, Q. Z. Cheng, Y. J. Zhou, Z. H. Liu, C. Y. Tao, *Water Sci. Technol.* **2019**, *79*, 366–374.
[46] A. D. Bokare, W. Choi, *Environ. Sci. Technol.* **2011**, *45*, 9332–9338.
[47] M. C. Fournier-Salaun, P. Salaun, *Cent. Eur. J. Chem.* **2007**, *5*, 1084–1093.
[48] G. Inzelt, *Encyclopedia of Applied Electrochemistry* (Eds.: G. Kreysa, K.-i. Ota, R. F. Savinell), Springer New York, New York, NY, **2014**, pp. 207–214.
[49] F. Y. Chen, Z. Y. Wu, Z. Adler, H. T. Wang, *Joule* **2021**, *5*, 1704–1731.
[50] L. Bousselmi, C. Fiaud, B. Tribollet, E. Triki, *Electrochim. Acta* **1999**, *44*, 4357–4363.
[51] a) I. Betova, M. Bojinov, T. Laitinen, K. Makela, P. Pohjanne, T. Saario, *Corros. Sci.* **2002**, *44*, 2675–2697; b) Y. Fu, C. D. Dai, H. Luo, D. Y. Li, C. W. Du, X. G. Li, *Appl. Surf. Sci.* **2021**, *560*, 149854.
[52] G. L. Song, *Corros. Sci.* **2005**, *47*, 1953–1987.
[53] H. Parangusan, J. Bhadra, N. Al-Thani, *Emergent Mater.* **2021**, *4*, 1187–1203.
[54] Z. J. Zhang, T. C. Yuan, R. D. Li, *J. Alloys Compd.* **2021**, *864*, 158105.
[55] X. Kang, F. N. Yang, Z. Y. Zhang, H. M. Liu, S. Y. Ge, S. Q. Hu, S. H. Li, Y. T. Luo, Q. M. Yu, Z. B. Liu, Q. Wang, W. C. Ren, C. H. Sun, H. M. Cheng, B. L. Liu, *Nat. Commun.* **2023**, *14*, 3607.
[56] L. Grandy, M. Chaniolleau, R. Lacasse, J. Mauzeroll, *J. Electrochem. Soc. Interface* **2023**, *170*, 051502.

Manuscript received: November 9, 2023
Accepted manuscript online: February 18, 2024
Version of record online: ■■, ■■

Research Articles

Alloy Electrocatalysts

A. Wetzel, D. Morell, M. von der Au, G. Wittstock, O. Ozcan, J. Witt* **e202317058**

Transpassive Metal Dissolution vs. Oxygen Evolution Reaction: Implication for Alloy Stability and Electrocatalysis

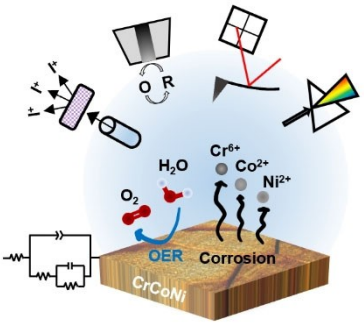

Multi-principal element alloys (MPEAs) have sparked significant interest for their corrosion and electrocatalytic stability. Investigating the CrCoNi alloy revealed substantial metal dissolution during the oxygen evolution reaction (OER) without typical corrosion indicators. This finding impacts MPEA stability understanding, emphasizing the need of precise OER catalyst efficiency measurements through metal ion quantification.